

The mass fallback rate of the debris in relativistic stellar tidal disruption events

T. JANKOVIČ¹ AND A. GOMBÖC¹

¹*Center for Astrophysics and Cosmology, University of Nova Gorica, SI-5000 Nova Gorica, Slovenia*

ABSTRACT

Highly energetic stellar tidal disruption events (TDEs) provide a way to study black hole characteristics and their environment. We simulate TDEs with the PHANTOM code in a general relativistic and Newtonian description of a supermassive black hole's gravity. Stars, which are placed on parabolic orbits with different parameters β , are constructed with the stellar evolution code MESA and therefore have realistic stellar density profiles. We study the mass fallback rate of the debris \dot{M} and its dependence on the β , stellar mass and age as well as the black hole's spin and the choice of the gravity's description. We calculate peak value \dot{M}_{peak} , time to the peak t_{peak} , duration of the super-Eddington phase t_{Edd} , time $t_{>0.5\dot{M}_{\text{peak}}}$ during which $\dot{M} > 0.5\dot{M}_{\text{peak}}$, early rise-time τ_{rise} and late-time slope n_∞ . We recover the trends of \dot{M}_{peak} , t_{peak} , τ_{rise} and n_∞ with β , stellar mass and age, which were obtained in previous studies. We find that t_{Edd} , at a fixed β , scales primarily with the stellar mass, while $t_{>0.5\dot{M}_{\text{peak}}}$ scales with the compactness of stars. The effect of SMBH's rotation depends on the orientation of its rotational axis relative to the direction of the stellar motion on the initial orbit. Encounters on prograde orbits result in narrower \dot{M} curves with higher \dot{M}_{peak} , while the opposite occurs for retrograde orbits. We find that disruptions, at the same pericenter distance, are stronger in a relativistic tidal field than in a Newtonian. Therefore, relativistic \dot{M} curves have higher \dot{M}_{peak} , and shorter t_{peak} and t_{Edd} .

Keywords: Black hole physics(159) — Hydrodynamical simulations(767) — Relativistic fluid dynamics(1389)
 — Tidal disruption(1696)

1. INTRODUCTION

The majority of galactic centers contain a supermassive black hole with mass M_{bh} in the range of 10^5 – $10^{9.5}$ M_⊙, surrounded by a central stellar cluster. There is a probability of about 10^{-5} – 10^{-4} /galaxy/year that a star from such a cluster is scattered and brought in the proximity of the black hole (Stone 2015; Alexander 2017). The star with mass M_* and radius R_* is disrupted if it enters the tidal zone, a region where black hole's tidal forces overcome stellar self-gravity. In the case of a non-rotating SMBH, tidal zone can be approximated as a sphere with a radius equal to the tidal radius $R_t = R_* (M_{\text{bh}}/M_*)^{1/3}$. The fate of the stellar debris depends on its total energy. Parts of the debris with positive energy are unbound and escape from the gravitational potential of the black hole. Conversely, debris with negative total energy is bound and returns to the black hole's vicinity, where it can form an accretion disk, which may emit radiation for months to years.

taj.jankovic@ung.si

Currently there are ≈ 100 observed TDEs (Komossa 2015; van Velzen & et al. 2019). This number is expected to increase drastically (≈ 1000 new sources per year) with the start of new wide-field optical surveys (e.g. Vera Rubin observatory) (van Velzen et al. 2011; Bricman & Gomboc 2020). In order to distinguish TDEs from other sources with similar locations (galactic center) or light curves, such as active galactic nuclei and supernovae, and to determine TDE parameters, accurate observations and detailed theoretical models are needed.

In the 80's and 90's, the first theoretical studies led to the discovery of various mechanisms of the disruption and the debris fallback phase (Carter & Luminet 1982; Rees 1988). TDEs were also studied with numerical simulations. First simulations were based on affine models (Carter & Luminet 1985) or on SPH codes (Evans & Kochanek 1989). SPH simulations were severely hindered by a low resolution since the number of particles was several orders of magnitude lower than what is used nowadays. For instance, Evans & Kochanek (1989) used $\sim 10^4$ particles, while current simulations use $\sim 10^6$ particles (Liptai et al. 2019). Initial studies were mainly focused on the disruption phase, however, as

technology advanced with time, studies focused also on later stages — on the return of the bound debris to the SMBH’s vicinity, and the formation and evolution of the accretion disk (Ayal et al. 2000; Hayasaki et al. 2013; Bonnerot et al. 2015; Liptai et al. 2019; Clerici & Gomboc 2020).

We focus on an analysis of disruptions of stars with realistic stellar profiles in a gravitational potential of a SMBH, which is described in general relativity (relativistic TDEs). A detailed study of relativistic TDEs of realistic main sequence stars was performed by Ryu et al. (2020a,b,c,d). Other previous studies have focused on TDEs in a simplified description of SMBH’s gravity, such as pseudo or generalized Newtonian potentials, and/or on disruptions of polytropic stars e.g. Hayasaki et al. (2013); Tejeda & Rosswog (2013); Guillouchon & Ramirez-Ruiz (2013); Gafton & Rosswog (2019); Golightly et al. (2019); Law-Smith et al. (2020). However, both the importance of general relativity and the accurate description of the stellar density profile are expected to play an important role. By simulating relativistic disruptions of realistic stars it would be possible to determine the deviation from previous results, obtained in a Newtonian gravitational potential or with simpler stellar models.

We simulate relativistic disruptions of realistic stars for different stellar and orbital parameters, and calculate the mass fallback rate of the debris \dot{M} . \dot{M} is often assumed to be directly related to the observed light curve (Rees 1988; Guillouchon & Ramirez-Ruiz 2013; Law-Smith et al. 2019). The reason for this assumption is a \dot{M} decay $\propto t^{-5/3}$, a relation analytically derived by Rees (1988) and also observed in TDE light curves (Komossa 2015; van Velzen et al. 2021). Furthermore, this is supported by several simulations, which indicate short disk circularization times and therefore confirm the tight relation between the fallback rate and the energy dissipated in the disk (Bonnerot et al. 2015; Liptai et al. 2019).

We compare the results from relativistic disruptions to results from non-relativistic simulations (in a Newtonian description of SMBH’s gravity) and characterize the effect of SMBH’s rotation on the \dot{M} . We also determine the differences between \dot{M} of realistic stars with various ages and masses.

This paper is organized as follows. In Section 2 we describe our method and in Section 3 we provide our results. In Section 4 we discuss the results and potential caveats. Section 5 summarizes our main conclusions. In Appendix we provide parameters of codes used in our simulations and the resolution test.

2. METHOD

We explore the disruption parameter space by simulating disruptions with different values of the stellar mass M_* , age, parameter β and SMBH’s spin a . Realistic stellar profiles are

obtained with the stellar evolution code MESA (Paxton et al. 2010) and are converted to a 3D particle distribution with the program MESA2HYDRO (Joyce et al. 2019). The process of disruption is simulated with the version v2021.0.0 of the PHANTOM software (Price & et. al. 2018).

2.1. Simulations

We present results from 52 simulations of stellar tidal disruption events in a relativistic (GR) and 30 simulations in a non-relativistic (NR), Newtonian, gravitational field of the SMBH. We use a stellar evolution software MESA and construct stars with masses $M_* = 0.6, 1, 2, 3 M_\odot$ at the beginning of the main sequence (zero age main sequence — ZAMS) and at the end of the main sequence (terminal age main sequence —TAMS). ZAMS is defined with the condition that 99% of the total energy is generated in nuclear reactions (fusion of hydrogen into helium), while the condition for TAMS is that the relative abundance of hydrogen in the core is lower than 0.1%. Stars with $M_* = 0.6 M_\odot$ have a lifespan longer than the age of the Universe. Therefore, we use a different TAMS condition for these stars — we stop the stellar evolution 10 Gyr after ZAMS. In all cases we assume initial solar metallicity.

MESA generates a 1D density profile, which has to be converted to a particle distribution in order to be correctly processed by PHANTOM. For this purpose we use the MESA2HYDRO code (Joyce et al. 2019). MESA2HYDRO distributes equal mass particles in concentric shells according to the desired density profile. The most interior part is modelled as a sink particle¹. The full extent of parameters used in MESA, MESA2HYDRO and PHANTOM is presented in Appendix A. We generate stellar distributions with $\approx 10^6$ particles and relax them for ≈ 20 dynamical timescales — we run these simulations in the absence of an external gravitational field (only stellar self-gravity) in order to dampen velocity perturbations of particles. We also perform a resolution test (see Appendix B) and find that our choice of the particle number is appropriate.

Relaxed stars are placed in parabolic orbits at a distance $5R_t$ from the SMBH with mass $M_{\text{bh}} = 10^6 M_\odot$. For GR simulations we calculate the initial positions and velocities according to a relativistic description adapted from the Appendix in Tejeda et al. (2017). In the case of NR simulations, we use a combination of Kepler’s orbit equation and the energy equation of a parabolic orbit. For each stellar mass, we consider up to 4 different values of the parame-

¹ A sink particle interacts only gravitationally with the other particles. It is used in the most central stellar region where the density can be several orders of magnitude larger than the density in outer layers. By modelling the stellar center with a single particle, sink particle, it is possible to avoid modelling stellar center with a high number of equal mass particles.

ter $\beta \equiv R_t/r_p = 1, 3, 5, 7$, defined as the ratio between the tidal radius R_t and the pericenter distance r_p . Due to our initial setup, stars with the same age, mass and β have the same r_p in GR and NR. We use an adiabatic equation of state with $\gamma = 5/3$, which corresponds to a gas pressure dominated regime. We stop the simulations between the first and second passage — after the disruption of the star and before the most bound debris returns to the proximity of the SMBH. For the majority of encounters, this corresponds to approximately 55 h after the disruption occurs. We note that for higher β the second passage happens sooner and simulations were stopped earlier. The effect of SMBH's rotation is taken into account by considering values of the SMBH's spin $a = \pm 0.99$. We use $a > 0$ when the star is on a prograde orbit — when the direction of the initial stellar motion and SMBH's rotation are aligned. Retrograde orbits are defined as $a < 0$. For encounters with $\beta = 1$ the effect of SMBH's rotation on the process of disruption is negligible. We consider disruptions of stars on non-inclined orbits — on orbits in the SMBH's equatorial plane. Table 1 lists the parameter space of simulated disruptions in this work².

2.2. Postprocessing

When a star enters SMBH's tidal field it is squeezed in the direction orthogonal to the orbital plane and in the radial direction due to the tidal field. This increases the stellar internal pressure. When the acceleration due to the gas pressure overcomes the acceleration due to the tidal squeezing, the collapsing layers bounce back, and the disruption occurs. The SMBH's tidal field affects the debris's energy distribution, which we use for calculations of the mass fallback rate of the debris — we adopt a similar procedure as [Lodato et al. \(2009\)](#); [Guillochon & Ramirez-Ruiz \(2013\)](#); [Gafton & Rosswog \(2019\)](#); [Law-Smith et al. \(2020\)](#); [Ryu et al. \(2020b\)](#).

We calculate the total specific energy (expressed in units of the particle mass) of the debris in non-relativistic encounters as

$$\epsilon = \epsilon_{\text{kin}} + \epsilon_g = \frac{1}{2}v^2 - \frac{GM_{\text{bh}}}{r}. \quad (1)$$

Here G is the gravitational constant, r is the radial distance to the SMBH and v is the size of the velocity vector.

In relativistic encounters we calculate ϵ in Boyer-Lindquist (BL) coordinates as in the Appendix in [Tejeda et al. \(2017\)](#). In units $G = c = 1$ the expression for the total specific energy is

$$\epsilon = \Gamma \left(1 - \frac{2M_{\text{bh}}r}{\rho^2} \left[1 - a \left(\frac{x\dot{y} - y\dot{x}}{r^2 + a^2} \right) \right] \right), \quad (2)$$

² We do not consider $\beta = 7$ encounters for $M_* = 0.6$, because the orbits are plunging. We simulate TDEs with $a = -0.99$ only for encounters with $\beta = 3$ because for the majority of disruptions with a higher β a part of the stellar gas is on plunging orbits.

where $\rho^2 = r^2 + \frac{a^2 z^2}{r^2}$. The position is defined with x, y, z coordinates, which are calculated in the reference frame of the SMBH. Γ is the Lorentz factor expressed in BL coordinates as

$$\begin{aligned} \Gamma = \frac{dt}{d\tau} = & \left(1 - \dot{x}^2 - \dot{y}^2 - \dot{z}^2 - \right. \\ & - \frac{2M_{\text{bh}}r}{\rho^2} \left(\left[1 - a \left(\frac{x\dot{y} - y\dot{x}}{r^2 + a^2} \right) \right]^2 + \right. \\ & \left. \left. + \frac{[r^2(x\dot{x} + y\dot{y}) + (r^2 + a^2)z\dot{z}]^2}{r^2\Delta(r^2 + a^2)} \right) \right)^{-1/2} \end{aligned} \quad (3)$$

Here Δ is $\Delta = r^2 - 2M_{\text{bh}}r + a^2$.

We use the Equations (1) and (2) (expressed in SI units) to calculate ϵ , and the third Kepler's law to determine \dot{M} as³

$$\dot{M} = \frac{dM}{dt} = \frac{dM d\epsilon}{d\epsilon dt} = \frac{dM}{d\epsilon} \frac{1}{3} (2\pi GM_{\text{bh}})^{2/3} t^{-5/3}. \quad (4)$$

We obtain the mass distribution of the debris over total energy $dM/d\epsilon$ from the final snapshot of simulations. We use the iterative approach described in [Guillochon & Ramirez-Ruiz \(2013\)](#) to calculate the self-bound particles⁴ and exclude them from calculations of $dM/d\epsilon$. We fit $dM/d\epsilon$ distributions with B-spline functions in order to produce smooth \dot{M} curves. We note, that using the Equation (4) to calculate \dot{M} assumes that the properties of gas are "frozen-in", and the gas is moving on ballistic trajectories. This is not necessarily true if the stellar core survives the disruption and its gravitational potential breaks the "frozen-in" approximation. To check the validity of this approximation, we calculated \dot{M} from snapshots at different times after the disruption (all before the most bound debris returns to the SMBH's vicinity). We find, that the differences between them are negligible and conclude, that this approximation is valid also for disruptions with a surviving stellar core.

This approach enables the calculation of characteristic values of the \dot{M} curves:

- the value of the peak \dot{M}_{peak} ,
- time t_{peak} (from disruption until $\dot{M} = \dot{M}_{\text{peak}}$),
- duration of the super-Eddington phase t_{Edd} (during which $\dot{M} > \dot{M}_{\text{Edd}}$),

³ We have also tried using the same approach as in [Gafton & Rosswog \(2019\)](#) and calculated \dot{M} from the geodesics. We found negligible differences between the two methods.

⁴ In less disruptive encounters, e.g. with a low parameter β and/or disruptions of stars with a high central density, it is possible that the stellar core survives. We refer to particles that are bound to the stellar core (and not to the SMBH) as self-bound particles.

Table 1. Parameter space of all the simulations. "+" and "-" symbols correspond to disruptions by a rotating SMBH, with $a = 0.99$ and $a = -0.99$, respectively. Ratio between the central density and the average density $\rho_c/\bar{\rho}$ determines compactness of the star. Values of r_p correspond to pericenter distances of the star during the first passage.

$M_\star [\text{M}_\odot]$	$R_\star [\text{R}_\odot]$	Age [Gyr]	$\rho_c/\bar{\rho}$	β	r_p/R_\odot
0.6	0.56	0	33	1, 3, 5	65.6, 21.9, 13.1
				3 ⁻ , 3 ⁺ , 5 ⁺	18.2 ⁻ , 24.0 ⁺ , 16.5 ⁺
0.6	0.58	10	43	1, 3, 5	69.3, 23.1, 13.9
				3 ⁻ , 3 ⁺ , 5 ⁺	19.8 ⁻ , 25.2 ⁺ , 17.1 ⁺
1	0.86	0	56	1, 3, 5, 7	86.9, 29.3, 17.7, 12.8
				3 ⁻ , 3 ⁺ , 5 ⁺ , 7 ⁺	27.0 ⁻ , 31.1 ⁺ , 20.3 ⁺ , 16.3 ⁺
1	1.23	8.3	1363	1, 3, 5, 7	123.2, 40.7, 24.3, 17.2
				3 ⁻ , 3 ⁺ , 5 ⁺ , 7 ⁺	39.1 ⁻ , 42.1 ⁺ , 26.3 ⁺ , 19.9 ⁺
2	1.27	0	96	1, 3, 5, 7	100.0, 32.8, 19.4, 13.6
				3 ⁻ , 3 ⁺ , 5 ⁺ , 7 ⁺	30.7 ⁻ , 34.9 ⁺ , 21.8 ⁺ , 16.8 ⁺
2	2.54	1.0	2426	1, 3, 5, 7	201.7, 68.3, 41.5, 29.9
				3 ⁻ , 3 ⁺ , 5 ⁺ , 7 ⁺	67.3 ⁻ , 69.3 ⁺ , 42.8 ⁺ , 31.6 ⁺
3	1.57	0	58	1, 3, 5, 7	109.1, 36.2, 21.7, 15.5
				3 ⁻ , 3 ⁺ , 5 ⁺ , 7 ⁺	34.4 ⁻ , 37.7 ⁺ , 23.9 ⁺ , 18.3 ⁺
3	3.25	0.3	1908	1, 3, 5, 7	222.0, 75.5, 45.8, 32.9
				3 ⁻ , 3 ⁺ , 5 ⁺ , 7 ⁺	74.5 ⁻ , 76.4 ⁺ , 47.0 ⁺ , 34.5 ⁺

- duration $t_{>0.5\dot{M}_{\text{peak}}}$ (during which $\dot{M} > 0.5\dot{M}_{\text{peak}}$),
- characteristic rise-time τ_{rise} ,
- late-time slope n_∞ .

τ_{rise} is calculated by fitting a Gaussian function $\propto e^{-(t-t_{\text{peak}})^2/(2\tau_{\text{rise}}^2)}$ to the mass fallback rate of the debris $\dot{M}(t)$ (motivated by van Velzen & et al. (2019)) in a range between $0.2\dot{M}_{\text{peak}} \leq \dot{M}(t) \leq 0.8\dot{M}_{\text{peak}}$ for $t < t_{\text{peak}}$. n_∞ is obtained by fitting a power-law function $\propto t^{n_\infty}$ to the late-time portion of $\dot{M}(t)$ curves with no apparent breaking in the power-law dependency. Typically, this corresponds to a range between $\dot{M}(t) \lesssim 0.1\dot{M}_{\text{peak}}$ for $t > t_{\text{peak}}$.

For NR encounters \dot{M}_{peak} , t_{peak} and t_{Edd} can be scaled with the stellar mass and radius as

$$\dot{M}_{\text{peak}} \propto M_\star^2 R_\star^{-3/2}, \quad (5)$$

$$t_{\text{peak}} \propto M_\star^{-1} R_\star^{3/2}, \quad (6)$$

$$t_{\text{Edd}} \propto M_\star^{1/5} R_\star^{3/5}, \quad (7)$$

where a constant SMBH mass and a flat $dM/d\epsilon$ distribution are assumed (Stone et al. 2019; Law-Smith et al. 2020). We also note that a star on the main sequence roughly follows a mass-radius relation $R_\star \propto M_\star^1$ and $R_\star \propto M_\star^{0.5}$, for $M_\star \lesssim 1.5 \text{ M}_\odot$ and $M_\star \gtrsim 1.5 \text{ M}_\odot$, respectively (Lamers & M. Levesque 2017). The scaling exponent is higher for lower mass stars due to the increasing role of the convective envelope. The mass-radius relation is also affected by the stellar age — the scaling exponent is higher for TAMS than for ZAMS stars (Demircan & Kahraman 1991).

3. RESULTS

The mass fallback rate curves \dot{M} are determined by the mass distribution of the debris after the first passage. The mass distribution is affected by the strength of the encounter, stellar structure and SMBH's rotation. Therefore, each of these leave an imprint on the \dot{M} curves and it's characteristic properties. Throughout the rest of the paper we divide our analysis in 3 different categories:

- comparison between GR and NR simulations,
- effects of the initial orbit and stellar properties,
- effects of the SMBH's rotation.

For each of these categories we study the effect on the characteristic properties of \dot{M} .

3.1. The disruption phase

3.1.1. First passage

Figure 1 shows common center of mass distances r_{cm} during the first passage of 1 M_\odot stars for different ages, parameters β and SMBH's spins a . Minima of r_{cm} correspond to pericenter distances. Older stars (TAMS) have larger radii and therefore also larger tidal radii, which results in higher values of r_p . The effect of spin is visible albeit not very strong and the effect differs if stars are on prograde or retrograde orbits due to the relativistic spin-dependent pericenter precession. For the same value of β stars on retrograde orbits get closer to the SMBH, while the opposite occurs for stars on prograde orbits.

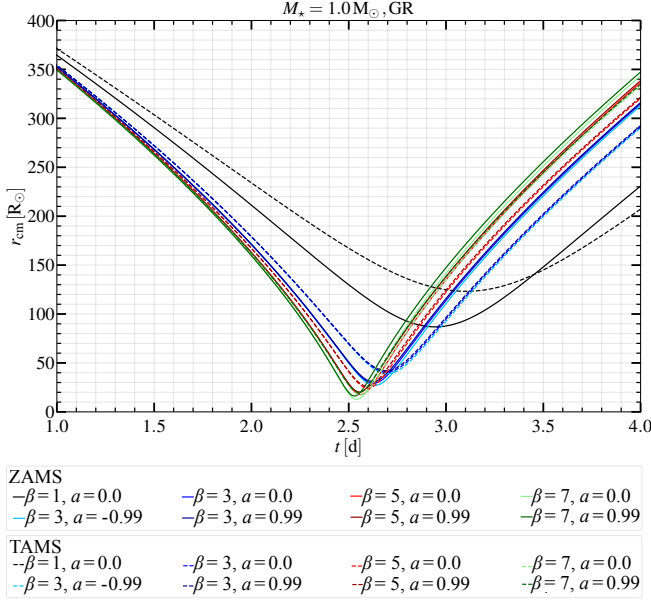


Figure 1. Common center of mass distances r_{cm} during the first passage for $1 M_{\odot}$ stars for different ages, β and a . Solid and dashed lines are used for r_{cm} of ZAMS and TAMS stars, respectively.

TDEs can be divided into 2 groups based on the amount of mass that remains bound to the stellar core after the disruption: partial (PTDEs) and total disruptions (TTDEs). These groups have different \dot{M} curves (Guillochon & Ramirez-Ruiz 2013; Gaftron & Rosswog 2019). For that purpose we define the *lost mass* $\Delta M/M_{\star}$, where $\Delta M = M_{\star} - M_{\text{self-bound}}$. Lost mass is a fraction of the total stellar mass that is not self-bound (bound to the possibly surviving stellar core) — a fraction that is “lost” to the SMBH (Guillochon & Ramirez-Ruiz 2013). Figure 2 illustrates dependence of the mass lost for all simulations. $\Delta M/M_{\star}$ increases with β and approaches a value of 1 when a TTDE occurs. We see that disruptions of ZAMS stars result in TTDEs (except for $\beta = 1$), while disruptions of older TAMS stars result in PTDEs (except for $\beta = 7$). This is partially a consequence of the definition of $\beta \equiv R_t/r_p$, where tidal radius depends on the size of the star. Furthermore, older stars have significantly more compact cores (see the ratio $\rho_c/\bar{\rho}$ in Table 1⁵) and therefore require a stronger encounter for a total disruption. On the other hand, stars with lower masses have a smaller tidal radius and are also more easily disrupted due to a less compact core. An

⁵ In general the value of $\rho_c/\bar{\rho}$ increases with the stellar mass and age. However, this trend reverses during the transition from a $2 M_{\odot}$ to a $3 M_{\odot}$ star. This is in agreement with Law-Smith et al. (2020) who observe a similar transition from $1.5 M_{\odot}$ to a $3 M_{\odot}$ star. The transition is a consequence of a formation of convective core for stars with $M_{\star} > 1.2 M_{\odot}$ (Lamers & M. Levesque 2017). In a stellar core convective mixing flattens the density profile.

exception are $3 M_{\odot}$ stars, that have lower values of $\rho_c/\bar{\rho}$ than $2 M_{\odot}$ stars (see Table 1). Therefore, $2 M_{\odot}$ stars are totally disrupted at a larger β than $3 M_{\odot}$ stars.

In general, relativistic disruptions result in a larger mass lost $\Delta M/M_{\star}$ for the same β compared to non-relativistic. We contribute this to a stronger tidal field in GR than in NR, and discuss this effect in Section 4. The amount of lost mass is also affected by SMBH’s rotation. A star on a retrograde orbit has a shorter pericenter distance and experiences a stronger tidal field, which results in a higher lost mass. On the other hand, the amount of lost mass is lower for disruptions of stars on prograde orbits.

3.1.2. Energy spread

The effect of tidal forces during the first passage results in an energy spread of the debris which in turn affects the \dot{M} curves. Mass distributions over total specific energy $dM/d\epsilon$ for $1 M_{\odot}$ simulations are shown in Figures 3 and 4. We show the distributions only for $\epsilon < 0$, where we do not include gas in the possibly surviving stellar core, because we are interested in the debris bound to the SMBH. We note, that distributions are symmetric with respect to the y -axis at $\epsilon = 0$ if the unbound gas is included. We mark the values of $dM/d\epsilon$ which correspond to the maxima of \dot{M} and to the time, when \dot{M} decrease below the Eddington limit (see Figure 6). We note that maxima of \dot{M} do not correspond to the maxima in $dM/d\epsilon$ distributions, since \dot{M} has also the term $d\epsilon/dt$ (see Equation 4). Although monotonically decreasing, the $d\epsilon/dt$ term shifts the peak values of \dot{M} curves towards more negative values of ϵ .

For PTDEs the distributions have a pronounced peak of $dM/d\epsilon$ as seen in Figure 3. Due to the exclusion of self-bound particles, values of $dM/d\epsilon$ sharply decrease as ϵ approaches 0. With increasing β the amount of matter bound to the stellar core is decreasing and the area integral of distributions increases until a TTDE occurs. Disruptions with higher β are stronger and the energy spread increases, which causes the debris to occupy a wider range of elliptical orbits after the disruption. The maxima of \dot{M} are shifted towards lower values of ϵ as the strength of encounters increases and a larger fraction of the debris is moving on more bound elliptic orbits⁶. For encounters with higher β the fallback rate of the debris becomes sub-Eddington at higher energies ϵ and therefore later times. Disruptions in GR are stronger than in NR, which results in wider energy distributions than NR (see Figure 4). At a fixed β the steepness of distributions at the low energy is similar in NR and GR, contrary to the energy

⁶ We note that in several high β disruptions the iterative approach, used to determine self-bound particles, yielded a self-bound mass within $\approx 0.05 M_{\star}$ even if there was no formation of a core-like structure. In those cases we assume a total disruption and extrapolate the last $\approx 10\%$ of $dM/d\epsilon$.

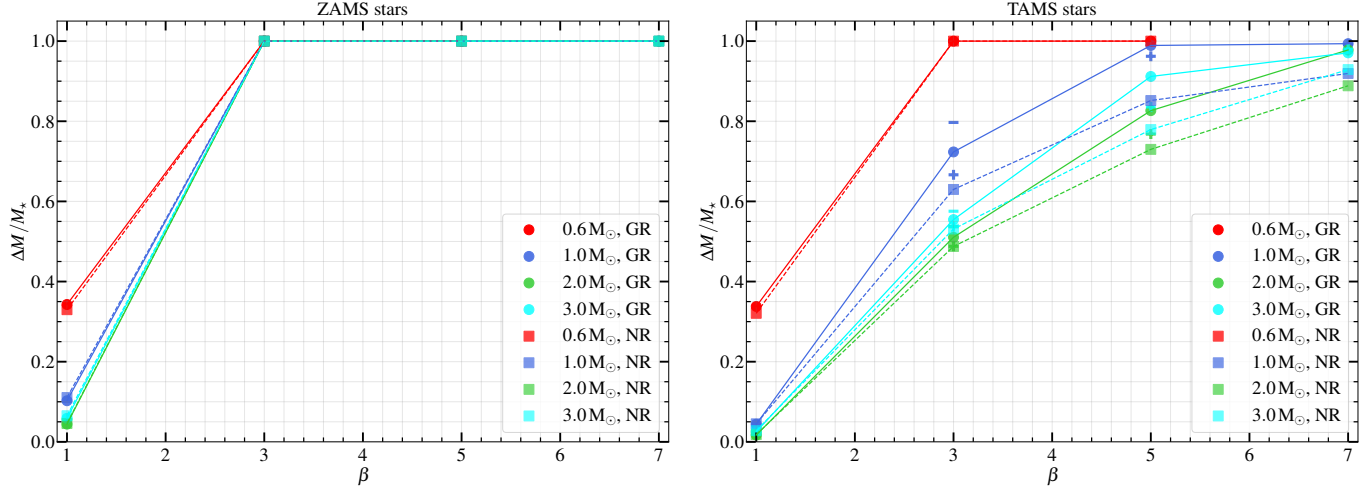


Figure 2. Fraction of the initial stellar mass that is not bound to the star for ZAMS (left) and TAMS (right) stars for different M_* , a and β . "+" and "-" symbols indicate results from disruptions of stars on prograde and retrograde orbits, respectively. Results for GR and NR simulations are indicated with "•" and "■" symbols, respectively. Values of $\Delta M/M_* \approx 1$ correspond to total disruptions.

distribution steepness at low energy for different β , where the steepness decreases with β .

SMBH's spin affects distributions of $dM/d\epsilon$ for prograde encounters in a similar way as decreasing β . For instance, $dM/d\epsilon$ distribution for a disruption of a ZAMS star with $\beta = 7$, $a = 0.99$ is more similar to $\beta = 5$, $a = 0$ than $\beta = 7$, $a = 0$. The opposite occurs for stars on retrograde orbits.

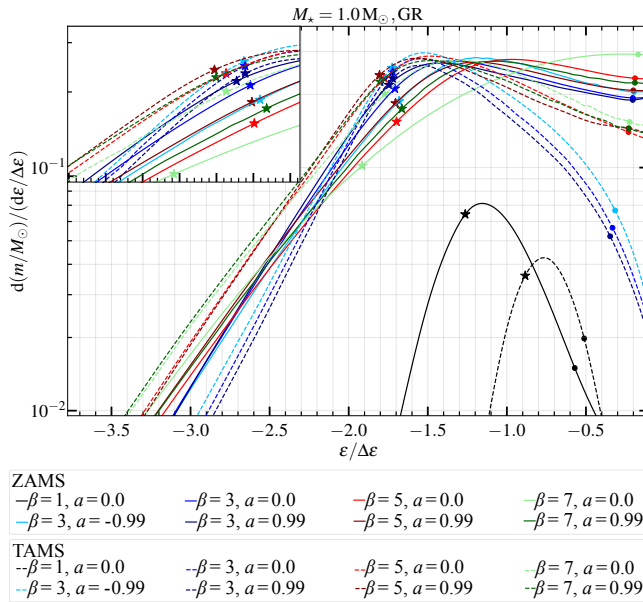


Figure 3. Mass distribution of the debris over total specific energy $dM/d\epsilon$ for $1 M_\odot$ calculated from the final snapshot of simulations. "*" symbols illustrate the values of $dM/d\epsilon$ that correspond to the maxima of \dot{M} , while "•" symbols represent the time when \dot{M} decreases below \dot{M}_{Edd} (see Figure 6). Solid and dashed lines correspond to results from disruptions of ZAMS and TAMS stars, respectively. Values of ϵ are normalized by $\Delta\epsilon = GM_{\text{bh}}R_*/R_t^2$.

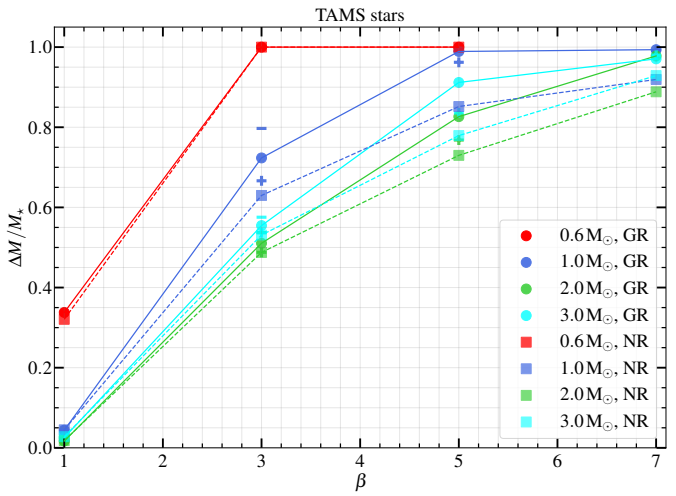


Figure 4. Mass distribution of the debris over total specific energy $dM/d\epsilon$ for $1 M_\odot$ ZAMS stars calculated from the final snapshot of simulations. "*" symbols illustrate the values of $dM/d\epsilon$ that correspond to the maxima of \dot{M} , while "•" symbols represent the time when \dot{M} decreases below \dot{M}_{Edd} (see Figure 6). Solid and dashed lines correspond to results from GR and NR disruptions, respectively. Values of ϵ are normalized by $\Delta\epsilon = GM_{\text{bh}}R_*/R_t^2$.

Consequences of the effect of tidal field are also visible in the debris configurations before the second passage. Figure 5 shows density slices of the debris $\approx 15t_{\text{dyn}}$ after the disruption of $1 M_\odot$ ZAMS (top row) and TAMS (middle row) stars in a NR and a GR gravitational field for various β . t_{dyn} is the dynamical times scale $t_{\text{dyn}} = (\sqrt{G\rho})^{-1}$. Disruptions in a relativistic gravitational field result in wider and more extended tidal streams in the orbital plane indicating that the

debris is moving on a wider range of elliptical orbits. This also indicates that the disruptions are stronger in a GR than in a NR gravitational field for the same β .

Older stars are more centrally concentrated and have less bound envelopes. Consequently, disruptions of these stars lead to debris configurations with more torqued and elongated tidal streams. The exception is the disruption of a ZAMS star for $\beta = 7$. In this case, the debris has been stretched almost to the maximum value due to the short orbital time scale and is on the verge of the second passage.

Figure 5 (bottom row) also illustrates the effect of SMBH's rotation on the debris configuration in the case of $1 M_\odot$ stars for $\beta = 3$. Disruptions of stars on retrograde orbits result in wider and more elongated tidal streams, similarly to stronger encounters. Furthermore, the effect of SMBH's rotation is more apparent in debris configurations of ZAMS stars. This is a consequence of shorter pericenter distances (for the same β) for younger stars — the importance of relativistic effects and effects due to the SMBH's rotation increases for closer encounters.

3.2. Mass fallback rate of the debris

The resulting \dot{M} curves are shown in Figure 6. The characteristic properties of the curves (\dot{M}_{peak} , t_{peak} , t_{Edd} , $t_{>0.5\dot{M}_{\text{peak}}}$, τ_{rise} , n_∞) differ significantly.

A detailed comparison of peak values \dot{M}_{peak} is seen in Figure 7. For NR encounters values of \dot{M}_{peak} are lower than for GR encounters with the same encounter parameters, which we contribute to a steeper gradient of the tidal field in GR. We note that the relative differences between NR and GR values of \dot{M}_{peak} increase with β as the pericenter distance decreases and the general relativistic effects increase.

From Equation (5) it is expected that \dot{M}_{peak} increases with the stellar mass at a fixed mass loss. This behaviour can be seen in values of \dot{M}_{peak} for ZAMS stars at $\beta = 3, 5, 7$ where TTDEs occur. We recover a similar dependence on the parameter β as Law-Smith et al. (2019) — \dot{M}_{peak} increases up to approximately $\beta \approx \beta_{\text{crit}}$, when a TTDE occurs, and then declines with a slower rate.

The effect of SMBH's rotation is seen in lower \dot{M}_{peak} values for total disruptions ($\Delta M/M_* \approx 1$) of stars on retrograde and higher for stars on prograde orbits. This effect is again similar to the dependency on the parameter β . In partial disruptions, the trend reverses: disruptions of stars on prograde orbits result in \dot{M} curves with lower peak values because the amount of lost mass decreases with a . The effect of SMBH's rotation is greater for closer encounters — for more massive stars and older stars at $\beta = 3$ the peak values of the fallback rate are within $\lesssim 2\%$, while for disruptions of ZAMS stars at $\beta = 7$ encounters the differences can be $\approx 15\%$.

3.2.1. Characteristic time scales

We calculate three different characteristic times: time to the peak t_{peak} , duration of the super-Eddington phase t_{Edd} (during which $\dot{M} > \dot{M}_{\text{Edd}}$) and duration $t_{>0.5\dot{M}_{\text{peak}}}$ (during which $0.5\dot{M}_{\text{peak}} < \dot{M} < \dot{M}_{\text{peak}}$).

In Figure 8 we see the results for t_{peak} (top row), t_{Edd} (middle row) and $t_{>0.5\dot{M}_{\text{peak}}}$ (bottom row). Due to a stronger SMBH's tidal field in a relativistic description of gravity there is more material on less energetic orbits (see Figure 4). GR TDEs produce fallback rate curves that reach peak values sooner, with a shorter duration of both t_{Edd} and $t_{>0.5\dot{M}_{\text{peak}}}$.

t_{peak} decreases with β , however, for $\beta \gtrsim \beta_{\text{crit}}$ it decreases at a slower rate. General trend of t_{Edd} and $t_{>0.5\dot{M}_{\text{peak}}}$ is that both quantities increase with the strength of disruption. In GR encounters of ZAMS stars t_{Edd} changes most drastically during the transition between PTDEs and TTDEs (by a factor of $\approx 2 - 4$) and continues to steadily increase with β . GR values of $t_{>0.5\dot{M}_{\text{peak}}}$ change by a maximum of factor ≈ 1.5 . t_{Edd} and $t_{>0.5\dot{M}_{\text{peak}}}$ of TAMS stars exhibit a similar pattern to ZAMS stars, with the exception being $t_{>0.5\dot{M}_{\text{peak}}}$ for $\beta = 1$. In this case durations of $t_{>0.5\dot{M}_{\text{peak}}}$ are substantially larger than for $\beta = 3$. We contribute this to larger pericenter distances during the disruptions of TAMS stars. As a consequence a larger amount of the debris is moving on more energetic orbits and $dM/d\epsilon$ curves are shifted towards more positive ϵ . This effect is only visible for disruption of TAMS stars on $\beta = 1$ orbits, where the pericenter distances can differ up to a factor of two from the pericenter distance of their ZAMS counterparts at $\beta = 1$. For larger β the mass over energy distributions span a more similar range of ϵ and consequently also more similar range of return times of the debris (see Figure 3).

At a fixed β less massive stars have shorter pericenter distances and experience a stronger tidal field. Therefore, the debris spans a wider range of elliptic orbits. However, more massive stars can have higher integrated values of M , depending on the amount of lost mass. In the case of TTDEs of ZAMS stars this effect is seen in longer t_{Edd} for more massive stars, which is also supported by Equation (7). On the other hand, t_{peak} decreases with the stellar mass, contrary to what one might expect from Equation (6). For TAMS stars, which have less bound envelopes and are mostly PTDEs, the interpretation of results is more intricate. For instance, at $\beta = 5$ a $1 M_\odot$ star gets closer to the SMBH than $2 M_\odot$ and $3 M_\odot$ stars and has a lower value of mass lost. As a consequence, it has a comparable t_{Edd} to a $2 M_\odot$ star. However, a $3 M_\odot$ star has more mass and a sufficiently larger (less bound) envelope, compensating for a weaker disruption due to a larger pericenter distance during the first passage, which results in a longer t_{Edd} than in the case of a $1 M_\odot$ star. A similar dependency on the stellar mass is observed in values

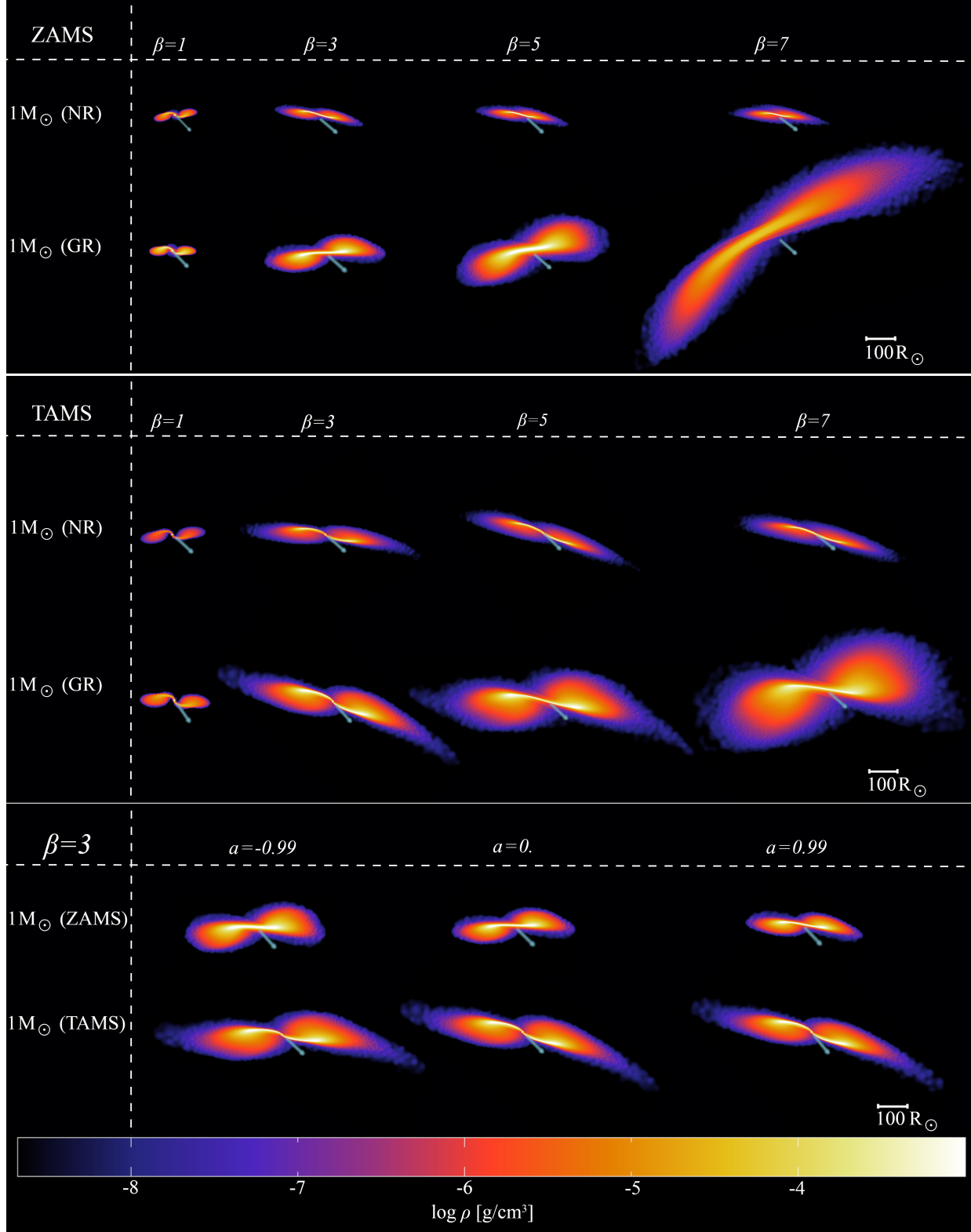


Figure 5. Density slices of TDE simulations of $1 M_{\odot}$ stars at $\approx 15 t_{\text{dyn}}$ after the pericenter passage. Arrows indicate the direction to the SMBH. We rotate slices of the debris configurations so that the directions towards the SMBH are aligned. *Top:* density slices of ZAMS stars after a disruption by a non-rotating SMBH with a Newtonian (first row) and a GR (second row) description of gravity. *Middle:* density slices of TAMS stars after a disruption by a non-rotating SMBH with a Newtonian (first row) and a GR (second row) description of gravity. *Bottom:* density slices of ZAMS (first row) and TAMS (second row) stars after a disruption by a rotating SMBH for $\beta = 3$.

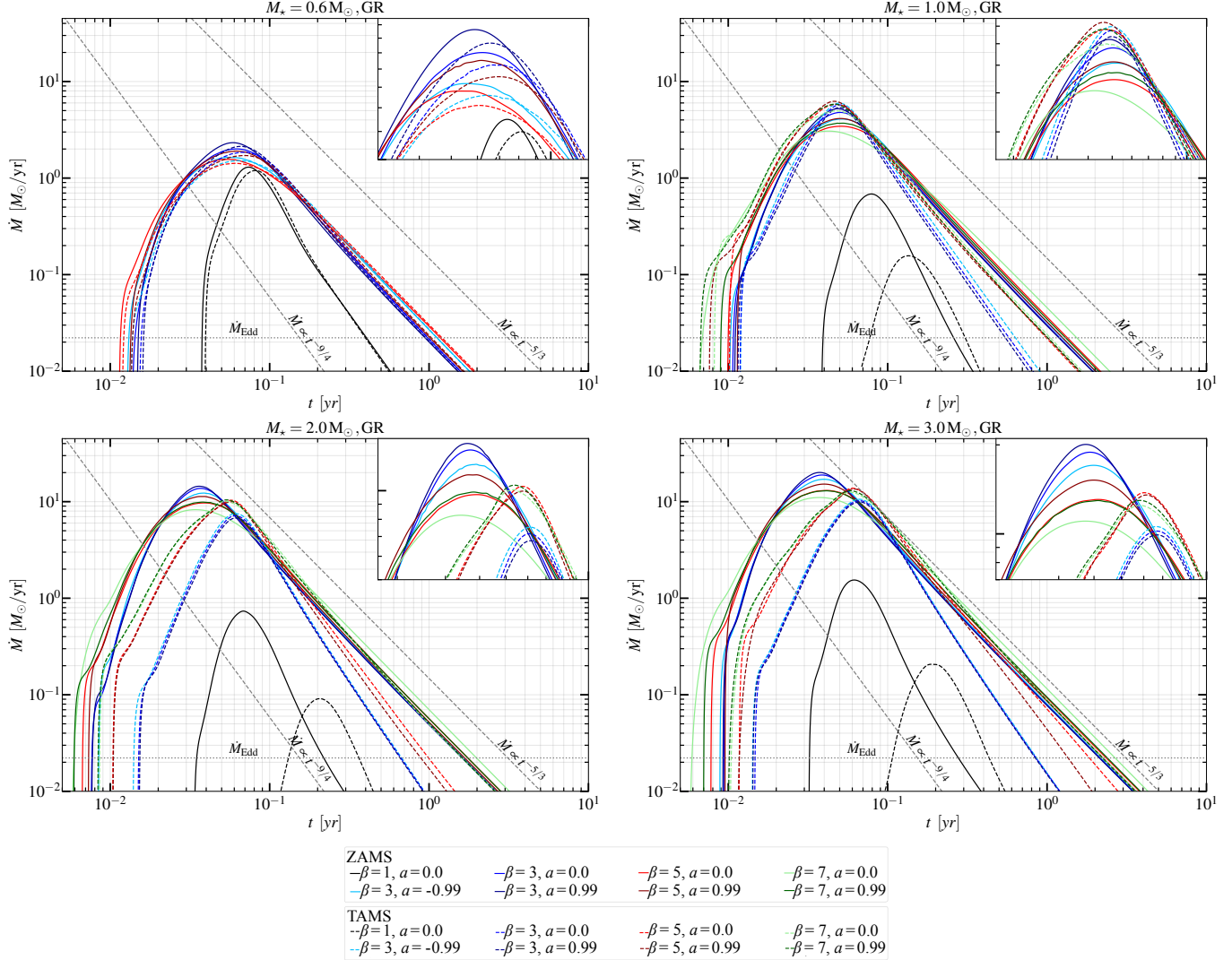


Figure 6. \dot{M} for stars with different masses and ages. Horizontal dotted line indicates the Eddington accretion rate of a $10^6 M_\odot$ SMBH. Diagonal dotted lines represent power-law curves: $t^{-5/3}$ for total stellar disruptions, and $t^{-9/4}$ for partial stellar disruptions. Boxes in the top right corners of individual plots show a zoomed-in region near the peak of \dot{M} curves.

of $t_{>0.5\dot{M}_{\text{peak}}}$ for TAMS stars. Disruptions of younger stars are mostly TTDEs and therefore result in higher values of t_{Edd} than for disruptions of older TAMS stars.

In disruptions of ZAMS stars SMBH's rotation induces shorter durations of t_{Edd} and $t_{>0.5\dot{M}_{\text{peak}}}$ for prograde and longer for retrograde stellar orbits. The effect of SMBH's rotation is less apparent in trends of t_{peak} for low β encounters. In high β encounters t_{peak} is longer for prograde orbits. Disruptions of TAMS stars by a rotating SMBH exhibit a similar trend to their ZAMS counterparts. The difference is that the results for rotating and non-rotating SMBH differ by a lower amount, due to a larger pericenter distance and consequently a lower effect of SMBH's rotation.

3.2.2. Early rise-time and late-time decline

We also calculate early characteristic rise-time τ_{rise} and late-time slope n_∞ . Obtained values are shown in Figure 9. Characteristic rise-time τ_{rise} is defined as the standard deviation of a Gaussian function fitted to the early part of \dot{M} curves, between 20 – 80% of \dot{M}_{peak} , and is analogous to the e-folding time. Therefore, lower values of τ_{rise} indicate a steeper rise of the fallback rate curves. Disruptions of stars in a relativistic tidal field lead to higher peak values of \dot{M} and shorter times to the peak. In agreement with this, we find that relativistic disruptions result in \dot{M} curves with lower values of τ_{rise} . An exception is the $2 M_\odot$ TAMS star at $\beta = 1$, which has a substantially longer t_{peak} and therefore longer τ_{rise} .

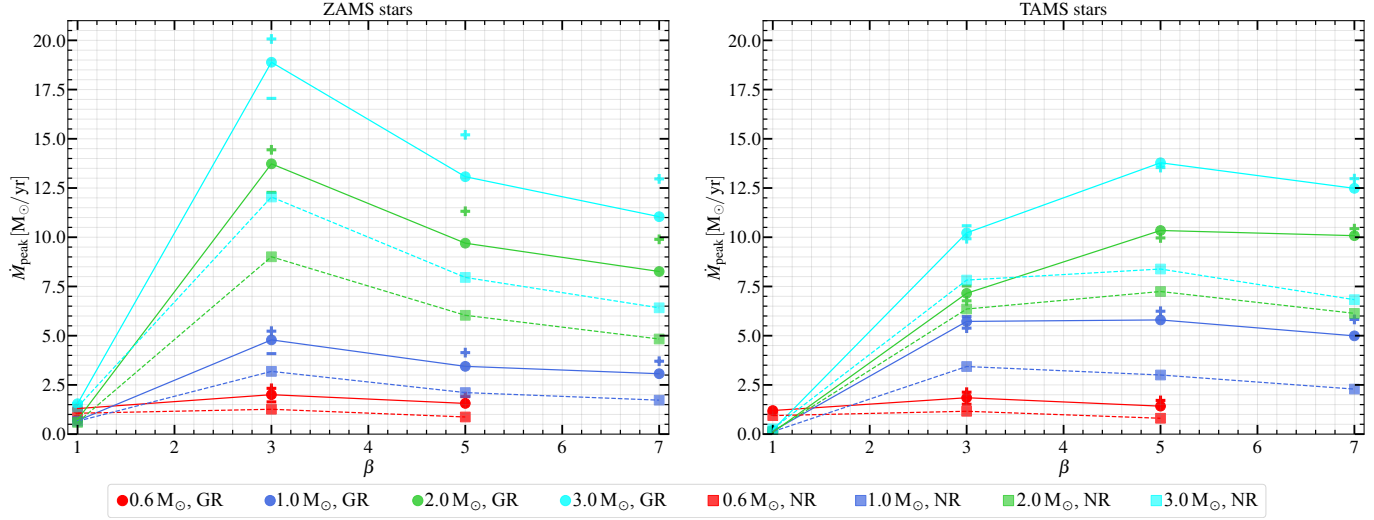


Figure 7. Peak values of \dot{M} for ZAMS (left) and TAMS (right) stars for different M_* , a and β . "+" and "-" symbols indicate results from disruptions of stars on prograde and retrograde orbits, respectively. Results for GR and NR simulations are indicated with "●" and "■" symbols, respectively.

As the strength of encounters increases, τ_{rise} becomes shorter. Furthermore, we find that disruptions of more centrally concentrated ZAMS stars (at a fixed β) lead to steeper rises of \dot{M} . In the case of partial disruptions of TAMS stars we find a different trend. TAMS stars have a lower density in the outer layers and these layers are more prone to disruption. As a consequence the debris is further stretched out and the density gradient in tidal tails is lower, which leads to a shallower rise slope. Furthermore, we find that the rotation of the black hole increases τ_{rise} for prograde orbits and decreases it for retrograde orbits.

For total disruptions n_∞ approaches $-5/3$, in agreement with previous numerical studies of the \dot{M} and theoretical predictions (Rees 1988; Guillochon & Ramirez-Ruiz 2013; Law-Smith et al. 2020). Theoretical analysis for partial disruptions predicts $n_\infty \approx -9/4$ (Coughlin & Nixon 2019). We find that for PTDEs there is a much larger scatter present around the predicted value. The SMBH's rotation can affect the late-time slope by both decreasing or increasing its value for the same β . However, we find no particular trend.

4. DISCUSSION

4.1. Disruptions in relativistic and Newtonian tidal fields

Kesden (2012) and Servin & Kesden (2017) study the differences between the energy spread in GR and in NR and give two possible explanations. Kesden (2012) argues that, for the same β , GR disruptions would be stronger and the energy spread would be larger. This would result in earlier peak times, higher M_{peak} and more narrow \dot{M} curves. However, Servin & Kesden (2017) argue that in GR a star would be disrupted further away from a SMBH, due to the steeper potential well. This would result in a smaller energy spread

in a relativistic tidal field and the effect on the \dot{M} would be the opposite — later peak times, lower M_{peak} and broader \dot{M} curves.

We determine the relativistic effects by comparing simulations of stellar disruptions at the same pericenter distances. In agreement with Kesden (2012) we find that disruptions in GR are stronger and produce a wider energy spread. The mass fallback rate of the debris reaches the peak value earlier and has a higher peak value. Furthermore, \dot{M} curves in GR have a narrower shape than in NR — values of t_{Edd} and $t_{>0.5M_{\text{peak}}}$ are lower in a relativistic tidal field. We find that the rise-time of relativistic \dot{M} is shorter.

Relativistic effects on the energy spread and \dot{M} were also studied by Cheng & Bogdanović (2014) and Gafton & Rosswog (2019). For a relativistic disruption of a $1 M_\odot$ polytropic star (for $\beta = 1$) by a $10^6 M_\odot$ SMBH Cheng & Bogdanović (2014) find that M_{peak} is higher by $\approx 2\%$ (we find $\approx 4\%$ for a ZAMS star), while t_{peak} and t_{Edd} are longer by $\approx 10\%$ and $\approx 7\%$, respectively, in comparison to NR encounters (we find that t_{peak} and t_{Edd} are shorter by $\approx 9\%$ and $\approx 10\%$, respectively, for a $1 M_\odot$ ZAMS star). Similar trend was also found by Gafton & Rosswog (2019). For comparison purposes we also simulate a NR and a GR disruption of a $1 M_\odot$ polytropic star for $\beta = 1$, and find the same trend as in disruptions of MESA stars. Therefore, we speculate that the discrepancies between our results and those by Cheng & Bogdanović (2014) and Gafton & Rosswog (2019) are not due to different stellar density profiles, but are caused by a different implementation of the self-gravity and/or the usage of a different TDE simulation software. Gafton & Rosswog (2019) used an SPH code with a pseudo-relativistic self-gravity description, Cheng & Bogdanović (2014) used a nu-

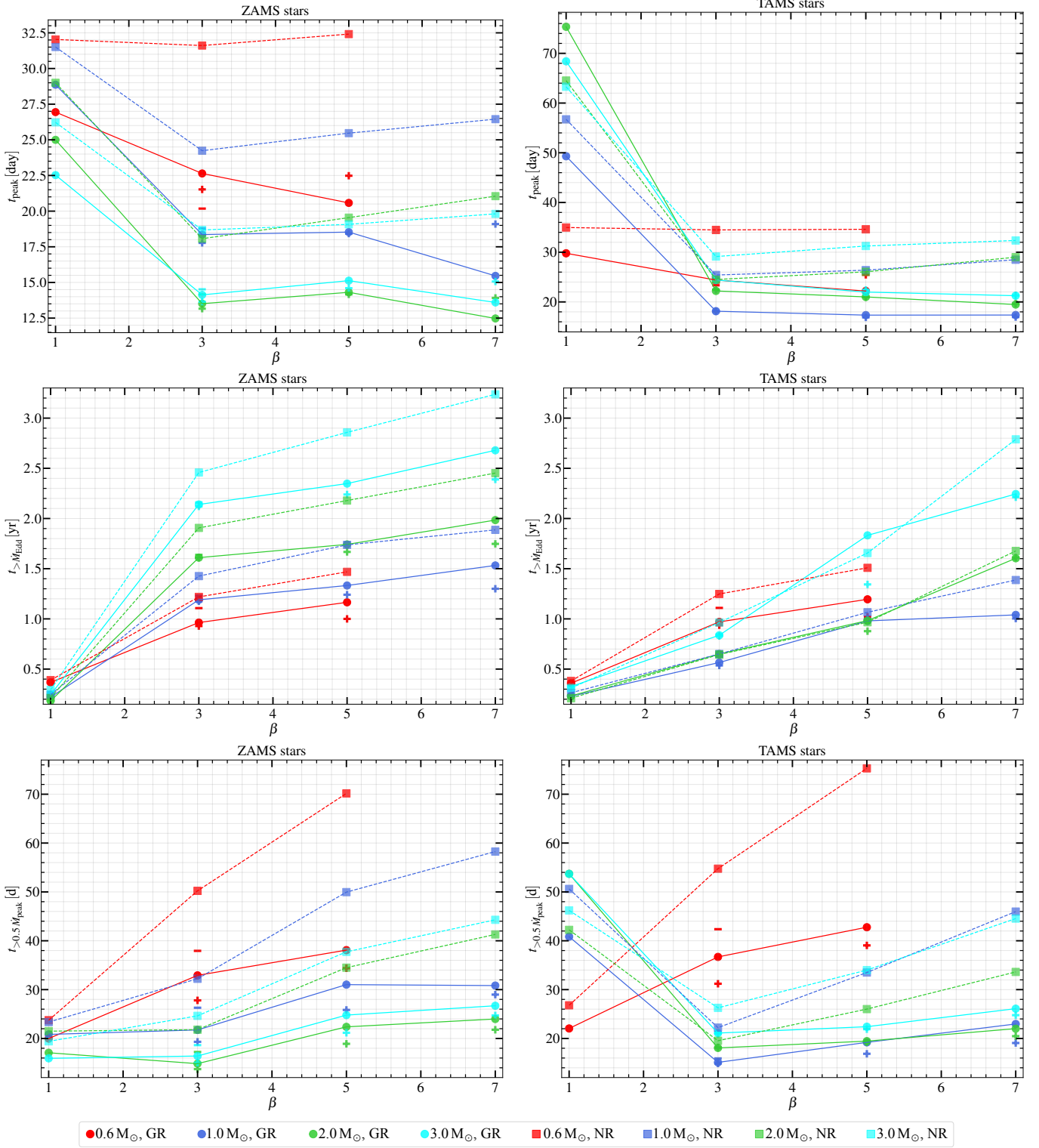


Figure 8. Characteristic time scales t_{peak} (top), t_{Edd} (middle) and $t_{>0.5M_{\text{peak}}}$ (bottom) for ZAMS (left) and TAMS (right) stars for different M_{\star} , a and β . "+" and "-" symbols indicate results from disruptions of stars on prograde and retrograde orbits, respectively. Results for GR and NR simulations are indicated with "●" and "■" symbols, respectively.

merical method that computes debris properties in a Fermi-normal coordinate system with the Newtonian self-gravity,

while we use an SPH code with a Newtonian self-gravity. We discuss this further in Section 4.4.

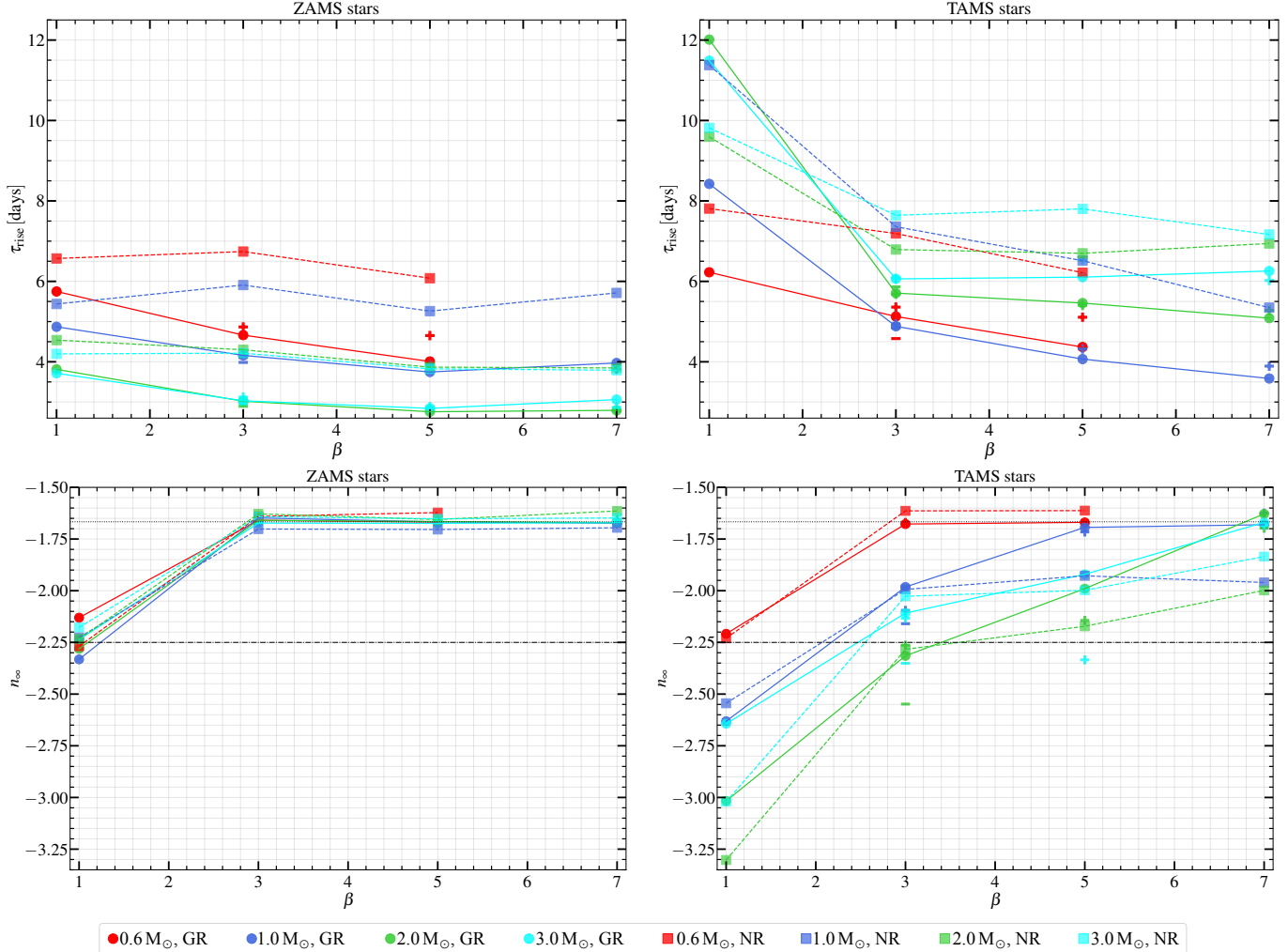


Figure 9. Early rise-time τ_{rise} (top) and late-time slope n_∞ (bottom) for ZAMS (left) and TAMS (right) stars for different M_* , a and β . "+" and "-" symbols indicate results from disruptions of stars on prograde and retrograde orbits, respectively. Results for GR and NR simulations are indicated with "●" and "■" symbols, respectively. For partial disruption the analytically predicted slope is $n_\infty \approx -9/4$ and for total disruption it is $n_\infty \approx -5/3$, which are represented with a dashed and a dash-dotted line, respectively.

Servin & Kesden (2017) and Stone et al. (2019) propose another approach to compare the differences between disruptions in GR and NR gravitational potentials. This is done by considering disruptions of stars with the same values of the specific angular momentum magnitude L . In this case it is expected that stars with the same angular momentum magnitude would experience stronger tides in GR at the pericenter. In our case, NR simulations have lower values of L than GR simulations at a fixed β . However, it is possible to compare GR and NR disruptions with a similar value of L by considering stellar orbits with a different β . For instance, a ZAMS star on an orbit with $\beta = 7$ in a relativistic gravitational field has a value of L similar (within $\approx 1\%$) to the one of a ZAMS star on an orbit with $\beta = 5$ in a Newtonian gravitational field. Therefore, by taking L as a proxy value for strength of the encounter (instead of the pericenter distance) we can com-

pare the characteristics of \dot{M} curves. For disruptions with the same value of L the relative differences between GR and NR values of \dot{M} characteristics are lower by a factor of ≈ 2 (in comparison to relative differences in disruptions at the same pericenter distance), while the trend remains the same. For instance, the relative difference in \dot{M}_{peak} is $\approx 43\%$ (instead of $\approx 76\%$), while the difference in t_{Edd} is $\approx 13\%$ (instead of $\approx 27\%$).

4.2. The effect of the SMBH's rotation

SMBH's rotation influences the initial stellar orbit by affecting the pericenter distance: pericenter distances of stars on retrograde orbits are decreased, while pericenter distances of stars on prograde orbits are increased. Therefore, stars on prograde orbits experience a smaller tidal field, which induces a smaller spread in energy of the debris. Consequently, \dot{M} curves of fully disrupted stars on prograde orbits have

lower values of ΔM , higher \dot{M}_{peak} , longer t_{peak} , are narrower (shorter durations of t_{Edd} and $t_{>0.5\dot{M}_{\text{peak}}}$) and have longer τ_{rise} . For partial disruptions (where the lost mass is $\Delta M \lesssim 0.8M_{\star}$) the effect of SMBH's rotation on the \dot{M}_{peak} is reversed, because SMBH's rotation changes the amount of lost mass. For larger ΔM trend is similar. However, the effect of the SMBH's rotation is much smaller due to larger pericenter distances. We note that the dependencies of all the characteristics of fallback rate curves on the SMBH's spin follow a similar trend to β dependency.

There have been only a few studies of the effect of SMBH's rotation on the mass fallback rate of the debris. The most extensive study, to our knowledge, is [Gafton & Rosswog \(2019\)](#). They simulated disruptions of polytropic stars by a spinning SMBH and calculated characteristic properties of \dot{M} , such as \dot{M}_{peak} , t_{peak} , t_{Edd} and n_{∞} . The general trend of the effect of SMBH's rotation is the same as found by us. \dot{M} curves for different values of the SMBH's spin were also calculated by [Kesden \(2012\)](#), who found that prograde spins reduce peak values of \dot{M} and delay t_{peak} . We recover the decrease in \dot{M}_{peak} in partial disruptions of TAMS stars. For high β encounters we find the opposite trend.

The black hole's rotation can also delay the start of the self-crossing, the self-collision between the part of the stream falling towards the SMBH and the part receding from the SMBH, which drives the subsequent accretion disk formation ([Liptai et al. 2019; Bonnerot & Lu 2020](#)). We stop our simulations before the most bound debris returns to the SMBH's vicinity and calculate \dot{M} as the mass return rate at the moment of the second passage. In this way, we avoid the uncertainties due to the nozzle shock⁷ and the self-crossing. For non-rotating SMBHs, self-crossing occurs after the second passage, but before the third passage ([Hayasaki et al. 2013; Bonnerot et al. 2015](#)). For rotating black holes, the relativistic Lense-Thirring precession induces a change in the nodal angle of the angular momentum of the receding stream, which causes a misalignment between the colliding streams in the self-crossing region ([Bonnerot & Stone 2020](#)). In most extreme cases the streams can even miss each other and collide after several revolutions, mainly between adjacent orbital windings ([Batra et al. 2021](#)). During each pericenter passage, \dot{M} can change due to the nozzle shock. However, [Jiang et al. \(2016\)](#) and [Bonnerot & Lu \(2021\)](#) find that the properties of the receding stream remain largely unaffected. This suggests that the mass fallback rate of the debris does not change significantly for adjacent windings and that our approach can be used to calculate \dot{M} also at a later time provided that the streams do not collide by that time.

⁷ During the pericenter passage, a strong vertical compression induced by an intersection of the inclined orbital planes of the returning gas results in a nozzle shock, which can change \dot{M} .

4.3. The effect of stellar and orbital parameters

\dot{M} curves vary with β , stellar mass and age. Careful analysis of these dependencies and construction of the fitting functions allow a more accurate calculation of characteristic properties from the observed lightcurve. Mostly, we recover similar trends as previous studies such as [Guillochon & Ramirez-Ruiz \(2013\); Ryu et al. \(2020b\); Law-Smith et al. \(2020\)](#). The dependencies can be divided into two main regimes: partial and total disruptions. These dependencies are directly related to the increase of the lost mass. Furthermore, the spread in energy is increasing with β , since the strength of the disruption increases as the pericenter distance decreases.

We confirm that the late-time slope in TTDEs is consistent with the theoretical prediction and follows $t^{-5/3}$. For PTDEs [Coughlin & Nixon \(2019\)](#) predicted a late-time decay $\propto t^{-9/4}$. We find a wide spread of power-law indices around the $n_{\infty} = -9/4$ value — differences between the calculated n_{∞} and predicted value by [Coughlin & Nixon \(2019\)](#) increase with the mass of the surviving stellar core.

4.3.1. Total disruptions

In total disruptions \dot{M}_{peak} , t_{peak} and τ_{rise} decrease, while t_{Edd} and $t_{>0.5\dot{M}_{\text{peak}}}$ increase with β for a fixed stellar mass. This is a consequence of a larger spread in energy of the debris as β increases and stars are disrupted in a steeper tidal field. After the disruption the orbits of the bound debris span a wider range of Keplerian ellipses. The most bound debris returns sooner to the proximity of the SMBH, while the least bound debris returns later for higher values of β . This effect is visible in shorter t_{peak} and longer t_{Edd} and $t_{>0.5\dot{M}_{\text{peak}}}$. Because for TTDEs the integral of \dot{M} over time needs to be constant, wider \dot{M} results in lower \dot{M}_{peak} .

At a fixed β , values of \dot{M}_{peak} and t_{Edd} increase, while the values of all the other characteristics decrease with M_{\star} (or with $\rho_c/\bar{\rho}$) in TTDEs. This can be understood from Equations (5) and (7) — for main sequence stars both quantities increase with M_{\star} . For t_{peak} Equation (6) predicts an increase with M_{\star} (for $M_{\star} \lesssim 1.5 M_{\odot}$) and a decrease with M_{\star} (for $M_{\star} \gtrsim 1.5 M_{\odot}$), when a mass-radius relation is taken into account. However, we find that t_{peak} decreases in the entire M_{\star} range in agreement with [Law-Smith et al. \(2020\)](#). An increase in peak values of \dot{M} and earlier peak times results in a shorter early rise-time scale. Furthermore, we find that $t_{>0.5\dot{M}_{\text{peak}}}$ decreases primarily with $\rho_c/\bar{\rho}$ and not M_{\star} .

4.3.2. Partial disruptions

In partial disruptions the dependence on β , M_{\star} and age is more nuanced — there is a general trend with several exceptions. Since PTDEs are mostly disruptions of TAMS stars, the stellar outer layers are less bound than in disruptions of ZAMS stars. Therefore, the effect on \dot{M} curves is determined by an interplay between the distance to the pericen-

ter (determines the strength of the encounter) and the ratio $\rho_c/\bar{\rho}$ (determines boundness of the outer layers). In order to more accurately determine how properties of \dot{M} curves scale with stellar and orbital parameters it would be better to verify their dependence on a parameter, which would be a function of β_{crit} (when a TTDE occurs) and $\rho_c/\bar{\rho}$. Law-Smith et al. (2020) propose $\exp(\beta/\beta_{\text{crit}})^{\alpha} - 1$, where $\alpha = (\rho_c/\bar{\rho})^{-1/3}$. However, determining β_{crit} is beyond the scope of this work.

\dot{M}_{peak} , t_{Edd} and $t_{>0.5\dot{M}_{\text{peak}}}$ are increasing with β at a fixed M_* , while t_{peak} and τ_{rise} are decreasing. At a fixed parameter β , values of \dot{M}_{peak} , t_{peak} , $t_{>0.5\dot{M}_{\text{peak}}}$ and τ_{rise} are increasing with M_* , similar to total disruptions.

4.3.3. Physical tidal radius

We determine parameter β from the tidal radius $R_t \propto \bar{\rho}^{-1/3}$, which does not depend on the stellar density profile. A more physical tidal radius $\mathcal{R}_t \propto (\rho_c/\bar{\rho})^{1/3}$ (for a fixed black hole mass), which determines the maximum pericenter distance for a total disruption, has been discussed in Ryu et al. (2020a). Therefore, it is possible to compare disruptions of different stars at the same physical parameter $\beta_p = \mathcal{R}_t/r_p$ by scaling the pericenter distance with the compactness $(\rho_c/\bar{\rho})^{1/3}$.

From Table 1 we estimate, that disruptions of $2 M_\odot$ and $3 M_\odot$ TAMS stars have, due to the higher compactness, shorter \mathcal{R}_t by a factor of ≈ 3 in comparison to their ZAMS counterparts. Therefore, partial disruption of a $2 M_\odot$ ZAMS star on an orbit with $\beta = 1$ has an equal β_p as partial disruption of a $2 M_\odot$ TAMS star on an orbit with $\beta = 7$ (the same holds also for $3 M_\odot$ ZAMS star and $3 M_\odot$ TAMS star on an orbit with $\beta = 1$ and $\beta = 7$, respectively). In Figure 10 we compare \dot{M} for these disruptions and find, that encounters of ZAMS stars result in a lower mass loss, while disruptions of TAMS stars are very close to TTDEs, contrary to results presented in Section 3. We see, that even though disruptions are scaled to the same β_p , the outcome is very different.

We also compare \dot{M} from a total disruption of a $2 M_\odot$ ZAMS star on an orbit with $\beta = 3$ and a total disruption of a $2 M_\odot$ TAMS star on an orbit with $\beta = 18.1$, where both encounters have an equal β_p . We find, that the outcome of the interaction between the SMBH and the star is substantially different already during the first passage. In the first case, there is no debris moving on plunging orbits, while in the second case, $\approx 10\%$ of the total stellar mass plunges in the SMBH. From these examples we conclude, that β and β_p cannot be used as clear indicators of an outcome of a TDE.

4.4. Potential caveats

Accurate self-gravity description is important in the treatment of various astrophysical phenomena. It is especially important in TDEs, e.g. in the calculations of \dot{M} because it affects the distribution of the debris mass over total energy after the disruption.

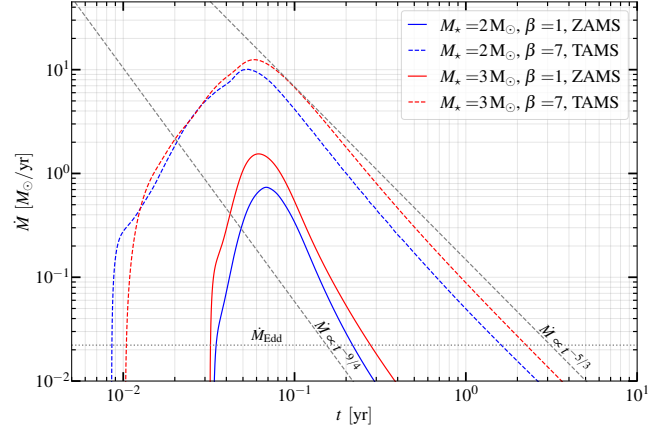


Figure 10. \dot{M} for $2 M_\odot$ and $3 M_\odot$ ZAMS and TAMS stars at the same physical parameter β_p (indicated by the same colors). Horizontal dotted line indicates the Eddington accretion rate of a $10^6 M_\odot$ SMBH. Diagonal dotted lines represent power-law curves: $t^{-5/3}$ for total stellar disruptions, and $t^{-9/4}$ for partial stellar disruptions.

The implementation of the self-gravity, the gravity between individual gas particles, is not trivial in relativistic simulations. In order to calculate the total force due to the self-gravity, experienced by a certain particle, it is necessary to determine the contribution from all other particles. Therefore, an accurate GR simulation would require Einstein's equations to be solved for each particle, which is not feasible with the current computational technology. In order to circumvent this problem, self-gravity is described in a Newtonian way or in a GR approximation (Gafton & Rosswog 2019; Ryu et al. 2020b).

In our simulations we use a Newtonian self-gravity, while Gafton & Rosswog (2019) and Ryu et al. (2020b) used different relativistic approximations. The research by Gafton & Rosswog (2019) is especially interesting, since their study also addressed relativistic effects on \dot{M} over a wide range of β . However, their results differ quantitatively as well as qualitatively from ours. This could be due to the only notable difference between their approach and ours, which we could identify — a different implementation of self-gravity⁸. Currently there is no method available, which would test the validity of the self-gravity implementation. The development of such a method is beyond the scope of this paper.

Another potential caveat is related to the conversion of the density profile obtained with MESA to a 3D density distribution of particles with the program MESA2HYDRO. This conversion results in a higher density in the stellar center due to the presence of a sink particle. Comparing values of $\rho_c/\bar{\rho}$

⁸ We note that they used a different SPH code and that they studied disruptions of a polytropic star. However, this does not explain the qualitative differences between our results.

from Table 1 to the values from Table 1 in Law-Smith et al. (2020) we see some discrepancies. Joyce et al. (2019) speculated that these discrepancies should not have any major consequences on the process of disruption. We confirm this by comparing several \dot{M} from NR disruptions to \dot{M} curves constructed with the STARS library (Law-Smith et al. 2020).

5. SUMMARY

We calculate mass fallback rate of the debris \dot{M} in a Newtonian and a general relativistic gravitational potential of a $10^6 M_\odot$ SMBH for different stellar masses M_* , ages, β parameter and SMBH's spins. We calculate peak values \dot{M}_{peak} , time to the peak t_{peak} , duration of the super-Eddington phase $t_{>\dot{M}_{\text{Edd}}}$, duration $t_{>0.5\dot{M}_{\text{peak}}}$, characteristic rise-time τ_{rise} and late-time slope n_∞ . Summary of our main results is:

- We recover the trends of \dot{M}_{peak} , t_{peak} , t_{Edd} , τ_{rise} and n_∞ with β , stellar mass and age, which were obtained in previous studies. We also find that the trends can change for stars with the mass $\approx 3 M_\odot$ stars due to the convective mixing, which decreases the central density.
- At a fixed β and stellar age, t_{Edd} increases with M_* , while $t_{>0.5\dot{M}_{\text{peak}}}$ increases with the compactness of stars $\rho_c/\bar{\rho}$.
- Comparison of \dot{M} from disruptions of stars (with the same M_* and different age) at an equal parameter $\beta \propto \bar{\rho}^{-1/3}$ or physical parameter $\beta_p \propto (\rho_c/\bar{\rho})^{1/3}$ is not a clear indicator of an outcome of a TDE.
- Disruptions at the same pericenter distance in a relativistic tidal field are stronger than in a Newto-

nian. This results in relativistic \dot{M} curves with higher \dot{M}_{peak} , and lower values of t_{peak} , τ_{rise} , t_{Edd} and $t_{>0.5\dot{M}_{\text{peak}}}$.

- Differences between a relativistic treatment of the SMBH's gravity and a non-relativistic are apparent even for $\beta = 1$ encounters. This emphasizes the importance to treat SMBH's gravity with a general relativistic description.
- For stars on prograde orbits, rotation of the SMBH results in a similar effect on \dot{M} as decreasing the pericenter distance, while the opposite happens for stars on retrograde orbits.

¹ This research was supported by the Slovenian Research Agency grants P1-0031, I0-0033, J1-8136, J1-2460 and the Young Researchers program. We acknowledge the use of MESA, MESA2HYDRO and PHANTOM for detailed hydrodynamical simulations and SPLASH for the visualization of the output (Paxton et al. 2010; Joyce et al. 2019; Price & et. al. 2018). We gratefully acknowledge the HPC RIVR consortium (www.hpc-rivr.si) and EuroHPC JU (eurohpc-ju.europa.eu) for funding this research by providing computing resources of the HPC system Vega at the Institute of Information Science (www.izum.si). We thank M. Joyce and E. Tejeda for the useful discussions. We are grateful to the anonymous referee for the comments and suggestions, which helped us improve the paper.

APPENDIX

A. PARAMETERS OF SIMULATIONS

Relevant parameters used in MESA, MESA2HYDRO and PHANTOM are shown in Tables 2, 3 and 4, respectively. MESA *inlist* files are available on Zenodo: [10.5281/zenodo.7428262](https://doi.org/10.5281/zenodo.7428262).

B. RESOLUTION TEST

We have performed a resolution test to determine if the results converge with the increasing number of particles N . We have performed simulations with $N \approx 5.1 \cdot 10^5$, $7.6 \cdot 10^5$, $1.0 \cdot 10^6$, $1.3 \cdot 10^6$. The results are shown in Figure 11. In the range of $\dot{M} \gtrsim 0.05\dot{M}_{\text{peak}}$ we find no noticeable differences between the results for different numbers of particles. There are minor discrepancies for low values of t for $\dot{M} \lesssim 0.05\dot{M}_{\text{peak}}$, at the order of $< 0.04t_{\text{peak}}$. Since t_{peak} is the shortest evaluated time scale in our study, we conclude that our results are sufficiently accurate.

Table 2. Relevant MESA parameters. For stars with masses $M_\star > 1.2 M_\odot$ we also take into account overshooting.

Parameter	Value
create_pre_main_sequence_model	.true.
new_net_name	'mesa_49.net'
new_rate_preference	2 !jina
kappa_file_prefix	'09'
initial_zfracs	6
kappa_lowT_prefix	'lowT_fa05_a09p'
initial_z	0.0142
initial_y	0.2703
Lnuc_div_L_zams_limit	0.999
mixing_length_alpha	2
delta_lg_XH_cntr_hard_limit	0.005
do_element_diffusion	.true.
xa_central_lower_limitspecies(1)	'h1'
xa_central_lower_limit(1)	0.001
maxovershoot_scheme(1)	'exponential'
overshoot_zone_type(1)	'any'
overshoot_zone_loc(1)	'any'
overshoot_bdy_loc(1)	'any'
overshoot_f(1)	0.014
overshoot_f0(1)	0.004

Table 3. Relevant MESA2HYDRO parameters.

Parameter	Value
IC_format_type	phantom_binary
r_depth	1e - 20
N	8
mp	1e - 6
stepsize	1e4
which_dtype =	d
TOL	0.01

Table 4. Relevant PHANTOM parameters. The softening length h_soft_sinksink of the sink particle is calibrated to be half of the innermost radius of the gas shells. We also use parameters GRAVITY = yes, ISOTHERMAL = no and, for GR simulations, GR = yes and METRIC = kerr.

Parameter	Value
alpha	1
alphau	0.1
beta	1
ieos	2
h_soft_sinksink	0.01188 (for $1 M_\odot$, ZAMS star)
accradius1	5
mass1	1
a	0. or 0.99

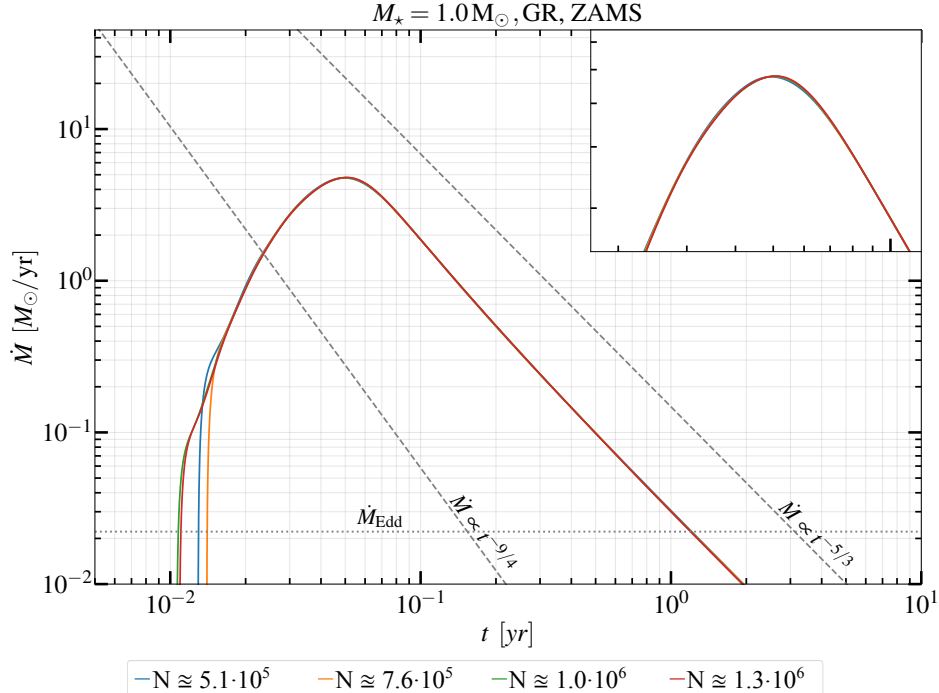


Figure 11. \dot{M} for $1 M_\odot$ ZAMS stars disrupted by a non-rotating SMBH for $\beta = 3$ and number of particles $N \approx 5.1 \cdot 10^5, 7.6 \cdot 10^5, 1.0 \cdot 10^6, 1.3 \cdot 10^6$. Horizontal dotted line indicates the Eddington accretion rate of a $10^6 M_\odot$ SMBH. Diagonal dotted lines represent power-law curves: $t^{-5/3}$ for total stellar disruptions, and $t^{-9/4}$ for partial stellar disruptions.

REFERENCES

- Alexander, T. 2017, Annual Review of Astronomy and Astrophysics, 55, 17–57, doi: [10.1146/annurev-astro-091916-055306](https://doi.org/10.1146/annurev-astro-091916-055306)
- Ayal, S., Livio, M., & Piran, T. 2000, The Astrophysical Journal, 545, 772, doi: [10.1086/317835](https://doi.org/10.1086/317835)
- Batra, G., Lu, W., Bonnerot, C., & Phinney, E. S. 2021, General Relativistic Stream Crossing in Tidal Disruption Events, arXiv, doi: [10.48550/ARXIV.2112.03918](https://arxiv.org/abs/10.48550/ARXIV.2112.03918)
- Bonnerot, C., & Lu, W. 2020, Monthly Notices of the Royal Astronomical Society, doi: [10.1093/mnras/staa1246](https://doi.org/10.1093/mnras/staa1246)
- . 2021, The nozzle shock in tidal disruption events. <https://arxiv.org/abs/2106.01376>
- Bonnerot, C., Rossi, E. M., Lodato, G., & Price, D. J. 2015, Monthly Notices of the Royal Astronomical Society, 455, 2253, doi: [10.1093/mnras/stv2411](https://doi.org/10.1093/mnras/stv2411)
- Bonnerot, C., & Stone, N. 2020, Formation of an Accretion Flow, arXiv, doi: [10.48550/ARXIV.2008.11731](https://arxiv.org/abs/10.48550/ARXIV.2008.11731)
- Bricman, K., & Gomboc, A. 2020, The Astrophysical Journal, 890, 73, doi: [10.3847/1538-4357/ab6989](https://doi.org/10.3847/1538-4357/ab6989)
- Carter, B., & Luminet, J. P. 1982, Nature, 296, 211, doi: [10.1038/296211a0](https://doi.org/10.1038/296211a0)
- Carter, B., & Luminet, J. P. 1985, MNRAS, 212, 23, doi: [10.1093/mnras/212.1.23](https://doi.org/10.1093/mnras/212.1.23)
- Cheng, R. M., & Bogdanović, T. 2014, PhRvD, 90, 064020, doi: [10.1103/PhysRevD.90.064020](https://doi.org/10.1103/PhysRevD.90.064020)
- Clerici, A., & Gomboc, A. 2020, Astronomy & Astrophysics, 642, doi: [10.1051/0004-6361/202037641](https://doi.org/10.1051/0004-6361/202037641)
- Coughlin, E. R., & Nixon, C. J. 2019, The Astrophysical Journal, 883, L17, doi: [10.3847/2041-8213/ab412d](https://doi.org/10.3847/2041-8213/ab412d)
- Demircan, O., & Kahraman, G. 1991, Ap&SS, 181, 313, doi: [10.1007/BF00639097](https://doi.org/10.1007/BF00639097)
- Evans, C. R., & Kochanek, C. S. 1989, The Astrophysical Journal, 346, L13, doi: [10.1086/185567](https://doi.org/10.1086/185567)
- Gafton, E., & Rosswog, S. 2019, Monthly Notices of the Royal Astronomical Society, 487, 4790–4808, doi: [10.1093/mnras/stz1530](https://doi.org/10.1093/mnras/stz1530)
- Golightly, E. C. A., Nixon, C. J., & Coughlin, E. R. 2019, The Astrophysical Journal, 882, L26, doi: [10.3847/2041-8213/ab380d](https://doi.org/10.3847/2041-8213/ab380d)
- Guillochon, J., & Ramirez-Ruiz, E. 2013, The Astrophysical Journal, 767, 25, doi: [10.1088/0004-637x/767/1/25](https://doi.org/10.1088/0004-637x/767/1/25)
- Hayasaki, K., Stone, N., & Loeb, A. 2013, Monthly Notices of the Royal Astronomical Society, 434, 909–924, doi: [10.1093/mnras/stt871](https://doi.org/10.1093/mnras/stt871)
- Jiang, Y.-F., Guillochon, J., & Loeb, A. 2016, The Astrophysical Journal, 830, 125, doi: [10.3847/0004-637x/830/2/125](https://doi.org/10.3847/0004-637x/830/2/125)

- Joyce, M., Lairmore, L., Price, D. J., Mohamed, S., & Reichardt, T. 2019, *The Astrophysical Journal*, 882, 63, doi: [10.3847/1538-4357/ab3405](https://doi.org/10.3847/1538-4357/ab3405)
- Kesden, M. 2012, *Phys. Rev. D*, 86, 064026, doi: [10.1103/PhysRevD.86.064026](https://doi.org/10.1103/PhysRevD.86.064026)
- Komossa, S. 2015, *Journal of High Energy Astrophysics*, 7, 148, doi: [10.1016/j.jheap.2015.04.006](https://doi.org/10.1016/j.jheap.2015.04.006)
- Lamers, H. J., & M. Levesque, E. 2017, *Understanding Stellar Evolution*, 2514-3433 (IOP Publishing), doi: [10.1088/978-0-7503-1278-3](https://doi.org/10.1088/978-0-7503-1278-3)
- Law-Smith, J., Guillochon, J., & Ramirez-Ruiz, E. 2019, *The Astrophysical Journal*, 882, L25, doi: [10.3847/2041-8213/ab379a](https://doi.org/10.3847/2041-8213/ab379a)
- Law-Smith, J. A. P., Coulter, D. A., Guillochon, J., Mockler, B., & Ramirez-Ruiz, E. 2020, Stellar TDEs with Abundances and Realistic Structures (STARS): Library of Fallback Rates. <https://arxiv.org/abs/2007.10996>
- Liptai, D., Price, D. J., Mandel, I., & Lodato, G. 2019, Disc formation from tidal disruption of stars on eccentric orbits by Kerr black holes using GRSPH. <https://arxiv.org/abs/1910.10154>
- Lodato, G., King, A. R., & Pringle, J. E. 2009, *Monthly Notices of the Royal Astronomical Society*, 392, 332, doi: [10.1111/j.1365-2966.2008.14049.x](https://doi.org/10.1111/j.1365-2966.2008.14049.x)
- Paxton, B., Bildsten, L., Dotter, A., et al. 2010, *The Astrophysical Journal Supplement Series*, 192, 3, doi: [10.1088/0067-0049/192/1/3](https://doi.org/10.1088/0067-0049/192/1/3)
- Price, D. J., & et. al. 2018, *Publications of the Astronomical Society of Australia*, 35, doi: [10.1017/pasa.2018.25](https://doi.org/10.1017/pasa.2018.25)
- Rees, M. J. 1988, *Nature*, 333, 523, doi: [10.1038/333523a0](https://doi.org/10.1038/333523a0)
- Ryu, T., Krolik, J., & Piran, T. 2020a, *The Astrophysical Journal*, 904, 73, doi: [10.3847/1538-4357/abbf4d](https://doi.org/10.3847/1538-4357/abbf4d)
- Ryu, T., Krolik, J., Piran, T., & Noble, S. C. 2020b, *The Astrophysical Journal*, 904, 98, doi: [10.3847/1538-4357/abb3cf](https://doi.org/10.3847/1538-4357/abb3cf)
- . 2020c, *The Astrophysical Journal*, 904, 100, doi: [10.3847/1538-4357/abb3ce](https://doi.org/10.3847/1538-4357/abb3ce)
- . 2020d, *The Astrophysical Journal*, 904, 101, doi: [10.3847/1538-4357/abb3cc](https://doi.org/10.3847/1538-4357/abb3cc)
- Servin, J., & Kesden, M. 2017, *PhRvD*, 95, 083001, doi: [10.1103/PhysRevD.95.083001](https://doi.org/10.1103/PhysRevD.95.083001)
- Stone, N. C. 2015, *The Tidal Disruption of Stars by Supermassive Black Holes* (Springer International Publishing), doi: [10.1007/978-3-319-12676-0](https://doi.org/10.1007/978-3-319-12676-0)
- Stone, N. C., Kesden, M., Cheng, R. M., & van Velzen, S. 2019, *General Relativity and Gravitation*, 51, doi: [10.1007/s10714-019-2510-9](https://doi.org/10.1007/s10714-019-2510-9)
- Tejeda, E., Gafton, E., Rosswog, S., & Miller, J. C. 2017, *Monthly Notices of the Royal Astronomical Society*, 469, 4483–4503, doi: [10.1093/mnras/stx1089](https://doi.org/10.1093/mnras/stx1089)
- Tejeda, E., & Rosswog, S. 2013, *Monthly Notices of the Royal Astronomical Society*, 433, 1930, doi: [10.1093/mnras/stt853](https://doi.org/10.1093/mnras/stt853)
- van Velzen, S., & et al. 2019, *The Astrophysical Journal*, 872, 198, doi: [10.3847/1538-4357/aafe0c](https://doi.org/10.3847/1538-4357/aafe0c)
- van Velzen, S., Farrar, G. R., Gezari, S., et al. 2011, *The Astrophysical Journal*, 741, 73, doi: [10.1088/0004-637x/741/2/73](https://doi.org/10.1088/0004-637x/741/2/73)
- van Velzen, S., Gezari, S., Hammerstein, E., et al. 2021, *The Astrophysical Journal*, 908, 4, doi: [10.3847/1538-4357/abc258](https://doi.org/10.3847/1538-4357/abc258)